Kenneth E. Perry[1], Alex Teiche[1]

Fatigue Crack Initiation in Superelastic Nitinol

Phase shifted moire interferometry is used to study fatigue initiation in superelastic Nitinol. Notched four-point bend coupon samples were fatigue tested according to a two a multi-level amplitude test protocol tailored for medical implant applications. Fringe patterns of local strain measurements are presented for three loading sequences based on the type of loading and range of anticipated strains in service. The effect of an initial series of pre-load cycles is examined and resulting life data is accompanied by local strain results highlighting the unique mechanisms associated with the initiation of fatigue cracks and the development of effective test methods and protocols.

KEY WORDS: *Nitinol, fatigue, crack, initiation, local, strain, gradient, phase transformation, multiaxial, constraint, plasticity, mean stress, dynamic, moiré interferometry*

Introduction

Fatigue failure is a common problem for repetitively loaded engineering structures [1], resulting primarily from the effects of local plastic strain. Fatigue crack initiation is generally described by strain life equations that relate the alternating strain amplitude to the number of cycles to crack initiation. The deformation behavior of superelastic Nitinol is complicated by a number of factors related to the unique phase transformation of the material leading to difficulties with quantifying the role of such factors as mean strain.

The fatigue life of metals is determined by assessing the relationship between local plastic strain amplitude and the number of cycles to crack initiation. These strain-life equations must account for the effects of mean strain, multiaxiality and cumulative damage [1]. These factors complicate fatigue life prediction for many engineering materials, especially for superelastic Nitinol.

Tabanli et.al. [2] were the first to explore the role of mean strain and demonstrate how it complicates the design of fatigue experiments for superelastic Nitinol. Pelton [3] provided an excellent review of the microstructure and fatigue mechanisms in superelastic Nitinol. The author concludes that the cyclic transformation between austenite and martensite is more complicated than elastic crystallographic theories would predict and emphasizes that optimized, thermo mechanically treated microstructures yield more stable (and predictable) behavior than annealed ones.

As described in [4], equivalent thermomechanical processing can be used to reproduce the desired material response from samples scaled to different physical dimensions. This approach has marked advantages: it equalizes both the material and process histories in addition to being a scaled representation of at least one mode of the structures anticipated in vivo loading.

---

[1]ECHOBIO LLC, 566 Stetson Place, Bainbridge Island, WA 98110

Most implants experience mixed-mode physiological loads in vivo and multiaxiality complicates establishing comprehensive fatigue models based on uniaxial material data. Runcimen et.al. [5] recently combined strain-life data from different loading modes using a modified Coffin-Manson approach where the number of cycles to failure was related to an equivalent alternating transformation strain. Data from different loading modes and testing conditions were combined. The approach performed well for low mean strains but was not satisfactory for conditions of high mean strain.

Cumulative damage (mentioned above) refers to the effects of load sequence and inelastic deformation history, local to a potential site for fatigue crack initiation. It is typical for medical implants made from superelastic Nitinol to experience one or more high amplitude loading cycles prior to low amplitude fatigue loading. Components may also have loading histories that intermix high-amplitude with low-amplitude cycles throughout the service life. The sequence of events in a component's loading history matter because of the different mean strains that can result in a transfer sequence from compression to tension and vice versa [6].

The ongoing challenge is to design robust superelastic Nitinol implant components and develop effective test methods to guarantee they will resist fatigue. Obtaining the appropriate cyclic stress strain behavior is necessary to relate applied strain test data to crack initiation periods in fatigue life models but this is complicated in superelastic Nitinol by local material phase transformation and plasticity.

A key element of our approach is to observe and characterize local notch root strain fields during fatigue. In this work we further extend the experimental technique of phase shifted moire interferometry [7, 8] to get in situ, full-field, local strain fields under controlled and instrumented cyclic load conditions, prior to and during fatigue crack initiation.

We use a specimen geometry optimized for superelastic Nitinol material and component studies (material, process and loading history). A single edge-notch at the outer fibers of the beam provides a strain concentrator, and non-zero (tensile-tensile) bending fatigue experiments are performed for samples, with and without initial high-amplitude pre-load cycles.

Materials and Methods

Specimen Geometry, Material and Loading Fixtures
A schematic of the specimen geometry is shown in Figure 1. The same specimen geometry has been designed and optimized for both axial and four-point bend fatigue loading. This configuration has been shown to achieve uniform tensile loading and pure bending over a large range of deformations.

The primary modification from [7] was the addition of a 0.3 mm notch at the center of the beam to provide a strain concentrator. As can be seen in the lower left of Figure 1, the redundant beam that would not be observed during the experiment has been removed.

The incoming material was seamless drawn superelastic SE-508 NiTi tubing from Nitinol Devices and Components, Inc., with an outer diameter of 5 mm and a 0.6 mm wall. Two pairs of 1 mm diameter holes, spaced 8.2 mm producing a 25 mm span were laser cut in the ends of the samples and then carefully honed to insure precision pin loading of the test samples. The pins in the outer holes of the sample were free to slide laterally in slotted holes

of the lower portion of the fixture. The pins for the inner holes were attached via linkages to the upper portion of the fixture.

The gage section of the samples were EDM'ed to produce perpendicular edges, maximizing the amount of material in the gage section and ensuring uniform behavior in bending. Slow feed, low power and multiple passes were used to minimize adverse effects on the bulk material properties. A flat surface was carefully ground on one face of the test samples to provide an optically flat surface for the grating replication process. The height of the gage section after grinding and polishing was 1.75 mm from top to bottom. At the neutral axis, the samples were 0.4 mm thick and at the outer fibers the thickness was 0.5 mm.

The sample was further ground and mechanically polished in the shoulder regions to eliminate strain concentrators that could compete with the notch. The tubing samples were thermomechanically processed with a single heat treatment at 500°C resulting in an active Austenite finish temperature (A_f) of 5°C. A final chemical polish consistent with typical medical implant processing specifications resulted in a uniform, reproducible surface finish for the test articles.

Crossed diffraction gratings were epoxy replicated from 300 l/mm holographic diffraction grating plates using conventional techniques [7, 9] with Micro-measurements (Raliegh, NC) M-Bond AE-10 adhesive kit. The final grating thickness of all of the samples was minimized and estimated to be 5–20 μm.

A grating density of 300 l/mm was chosen to maximize measurement sensitivity for the anticipated range of deformations. This resulted in a fringe order sensitivity of 1.67 μm/fringe.

The custom four point bend fixture used for the experiments is shown in Figure 2. The fixture utilized smooth, hardened steel pins secured with o-rings (shown removed) for attachment of the sample. Slots and the independent inner elements of the fixture minimize over-constraint of the sample and encourages a symmetrical deformation.

Loading Sequences and Fatigue Test Parameters

Three loading sequences were used to explore the fatigue initiation behavior of the four point bend samples. The first of these sequences, designated 'Ia', was a simple sinusoidal cycle with no pre-load. Samples tested according to this sequence were loaded from zero and cycled between the specified maximum and minimum fatigue displacement levels for that particular sample.

Samples tested according to the loading sequences designated 'IIa' and 'IIb' were also cycled between the maximum and minimum fatigue displacement levels, but received an initial 10 pre-load cycles. The difference between these two cases is the transfer sequence leading into the high cycle fatigue portion of the loading history.

For the case of IIa, the component is unloaded from peak applied loading directly into high cycle fatigue cycles. For the case of a IIb loading sequence, the sample is fully unloaded after the initial 10 pre-load cycles and high cycle fatigue cycles begin from an unloaded condition. Figure 3 illustrates the three loading sequences and defines the relevant loading levels.

To isolate the effects of the different loading sequences, it was important to utilize consistent testing parameters. Preliminary observations were used to select values for the peak pre-load level, the mean applied displacement, and the number of pre-load cycles to be performed were established.

The load/deflection behavior of several samples was observed in conjunction with live moire fringe patterns. A peak pre-load displacement of 0.6 mm was chosen because it was high enough to clearly initiate phase transformation on the free surface of the specimen under observation. Ten cycles at this fixed displacement amplitude did not produce obvious damage at the notch were applied for samples fatigue tested with initial high-amplitude cycles.

A mean displacement level sufficiently high to induce a mixed phase conditions was desired. A minor but consistently detectable change in the global load-deflection behavior for all of the samples was observed by 0.40 mm and a value of 0.45 mm was selected for the mean displacement level. This mean applied displacement level corresponded to a mean force of 18 N ±1 N for the sample during the initial loading cycle.

A first set of experiments was performed at the 0.45 mm fixed mean displacement to identify the 1M cycle applied strain amplitude for a 50% fracture rate and the associated standard deviation. Eighteen samples were fatigue tested without pre-load cycles with cyclic amplitudes selected using a D-optimal algorithm [10]. These data (not included herein) informed the selection of four discrete strain amplitudes for fatigue testing with high-amplitude pre-load cycles. Cyclic displacement levels of 0.8, 0.6 and 0.4 mm were chosen for the pre-load fatigue study. The Table below summarizes the test conditions for each loading sequence.

Loading Sequence	Pre-load Details	Mean Fatigue Loading Level	Samples Tested
Ia	no pre-loading	0.45 mm (18 N)	14
IIa	10 cycles, 0.0 − 0.6 mm cycled from peak load	0.45 mm (18 N)	10
IIb	10 cycles, 0.0 − 0.6 mm cycled from zeroload	0.45 mm (18 N)	10

Table 1: Summary of fatigue loading conditions.

Fatigue Test System and Data Acquisition

The samples were fatigue tested with a Bose 3230 ElectroForce test system (Eden Prairie, MN). Global measurements of the applied load were made using a 450 N range load cell and the crosshead transducer was used for displacement sensing and control. Figure 4 shows a photograph of the four point bending fixture mounted in the load frame. Calibration for all sensors was performed to ensure accurate measurements.

Displacement control was used for all loading conditions with amplitude compensation to maintain the specified limits during a test. Testing was conducted at a maximum of 20 Hz. Full field data was available at the maximum resolution of 1360x1024 up to 20 Hz cycling. Higher speeds can be achieved either by decreasing the resolution or taking data every Nth loading peak instead of every peak.

A thermocouple on the back side of the sample was used to monitor temperature of the samples during the experiments. This data was recorded along with load and deflection

for both timed data and peak valley acquisitions. All samples were tested under ambient conditions and confirmed to remain at 24°C, ± 1°C throughout all of the testing.

The experiments employed two personal computers, one each for the Bose test system and phase shifting moiré interferometer system. The first computer was responsible for controlling the load frame, and the acquisition of all non-moiré data. Load, cross-head deflection, cycle count and thermocouple measurements were digitized to 16 bits and routinely recorded at appropriate intervals during testing for all of the samples. A second computer manages the moiré interferometer, phase shifter, high speed camera and the control interface described above.

Local Strain Measurement

Moire interferometry provides in-plane displacement data in the form of sinusoidally modulated fringe patterns. The general technique is described in detail in [11]. Phase shifting extends the basic moire interferometry technique [12] by temporally oversampling the interference patterns and introducing a known phase shift into one of the beam paths. The sampled intensities and the known phase shift are used to create a significantly noise reduced "wrapped" fringe pattern with no loss of spatial resolution.

The interferometer used in these experiments was custom built with an integrated fiber optic splitter and phase shifter to provide exceptional stability and configurability [13]. The four beam interferometer head mounted on the optical table is shown in Figure 5. The horizontal pair of beams was used to produce the U-field fringe patterns and the pair of vertical beams was used for the V-field.

Digital images were recorded using the Qioptiq T-100 Optem telecentric 10x zoom lens and an Allied Vision Technologies, Canada, Inc. (Burnaby-BC) GC1380H Prosilica GC high speed camera. The specialized equipment has a range of high performance spatial resolution and frame rate combinations from 1360x1024/30 fps to 170x128/120 fps, both at 10 bit gray scale resolution.

A custom interface was written to integrate the cameras capabilities into the phase shifted moiré interferometry [12] software system. The interface integrates control of the camera and fiber phase shifter with two digital control lines from the dynamic test machine. The analog actuator output signal is rectified and used to hardware-trigger the camera, allowing frames to be captured at the min and max loading conditions. A user-controllable digital output is used to allow the fatigue testing control software to trigger taking phase shifted moiré interferometry data while the fatigue test machine is paused. Using the block configuration mode within the fatigue test machine software, the machine could fatigue the sample for a given time, pause the machine, start phase shifting and acquiring image data, and automatically restart cycling after the data was recorded. To permit fully automatic data collection the software includes an algorithm to estimate the signal to noise ratio of a wrapped image and reject those that fall below a quality threshold.

Max/min data was obtained one field at a time. A beam block, shown in Figure 4, was mechanically moved to isolate the individual fields. Five phase shifted, wrapped images were captured for each local displacement field measurement. Each image must go through an unwrapping process, which reconstructs a smooth representation of the underlying continuous displacement fields. After unwrapping each field goes through a repair process where any pixels that failed to be unwrapped due to artifacts on the diffraction grating are filled

in based on the values of the pixels around them. This prevents inaccurate data from propagating beyond the single pixel during the derivation stage. Before and after derivatives are taken a variable amount of smoothing is applied (but kept consistent within each data set). For any given load state, the process was repeated for both fields.

Results

Local Deformation and Strain Behavior

Figure 6 shows a series of images of a sample with a single edge notch loaded in tension. Wrapped fringe patterns of the U-field displacements on the left and surface images on the right are shown for increasing applied load up to the third row which corresponds to the peak pre-load. The fourth row shows the sample fully unloaded after the first pre-load cycle.

The caustic forming ahead of the notch root by the third row indicates regions of the sample surface experiencing high local strain. Phase shifting of the fringe patterns recovers enough signal such that fully resolved and differentiable strain fields were obtained even without the use of carrier fringes [7].

The loading depicted in Figure 6 is characteristic of the complete loading range for all of the samples tested. The applied displacement in the second row of Figure 6 was 0.45 mm and corresponds to the mean fatigue displacement level. There is some evidence of non-uniform local deformation in the surface image of the second row, but it is readily recovered upon unloading.

A contour plot of the maximum principal strain at the peak pre-load level for this sample is shown in Figure 7. Local strain as high as 3–3.5% is visibly concentrated on either side of the notch root centerline. The peak strain and general distribution compares favorably with results produced using finite element analysis (not included here).

In the final row, the sample has been fully unloaded. The horizontal fringes indicate uniform (zero) strain due to a uniform rigid body rotation. The shadow at the notch root can no longer be seen in the surface image, as the local deformation has been fully recovered and there are no signs of local residual deformation or damage on the surface of the sample.

Cyclic Amplitude and Crack Initiation Periods

Fifteen samples were fatigue tested without pre-load cycles around the nominal mean fatigue level of 0.45 mm. The median cyclic amplitude for 1M cycle survival was estimated to be 0.04 mm. Based on this value, a 1% fracture rate would be expected for a cyclic amplitude of 0.036 mm, with 99% of samples expected to initiate a fatigue crack at cyclic amplitudes greater than 0.044 mm.

Fatigue crack initiation periods for samples with pre-load cycles are compared in Figure 8 to the baseline data established for samples without pre-load cycles. All the data points were tested at the nominal mean fatigue level of 0.45 mm at the cyclic amplitudes indicated.

Initiation periods for samples tested with high-amplitude, pre-load cycles are shown as filled squares and circles in Figure 8, depending on whether fatigue the sample was directly cycled or fully unloaded after the high-amplitude pre-load. Cyclic amplitudes for samples with pre-load cycles were greater than those without. Samples that were fatigue tested directly after the pre-load cycles showed the strongest effect while those that were unloaded prior to fatigue testing showed more variability.

Fatigue Crack Initiation Without Pre-Load Cycles

For samples without high amplitude loading cycles, the deformation ahead of the notch was minimal. In many cases, there were no visible signs of damage or localization until just before a fatigue crack would appear at the notch. Initiation occured directly at the center of the notch, or slightly off to one side.

Figure 9 illustrates a fatigue crack initiating for a sample without pre-load cycles during a fatigue test conducted at 20 Hz. Phase shifted fringe patterns were acquired every 500 cycles, at both the maximum and minimum fatigue levels of the U-field displacements to observe the initiation of a fatigue crack. This sample was tested at a cyclic amplitude of 0.04 mm. Top row images correspond to a cycle count of approximately 62,500. Preceding image data was nearly identical, with uniform deformation and no localization on the face of the sample. Beginning in the second row, two caustics appear on either side of the centerline. By row three, the initiation site eventually favors the left side.

High resolution image data of a typical fatigue crack initiating from the notch is shown in Figure 10. This image was taken at the maximum fatigue level where five and one half fringes separate either side of the fatigue crack, corresponding to $9.2 \, \mu$m of displacement along the edge of the notch.

The local deformation becomes more complex ahead of the notch with the appearance of a secondary pattern of high frequency fringes and mixed material phases. Distinct boundaries between different material phases can be seen in the corresponding surface image. The two sharp interfaces bifurcate from the midline of the fatigue crack at angles of 53° and 58° from the loading axis.

Fatigue Crack Initiation With Pre-Load Cycles

Figure 11 shows the fatigue crack initiation of a sample at 102,000 cycles, tested with pre-load cycles at a cyclic amplitude of 0.08 mm. The top row was acquired at the maximum, and the bottom row at the minimum fatigue level during fatigue cycling at 20 Hz. The surface images reveal the nature and extent of local phase transformation around the notch throughout the the loading cycle.

Additional data was taken at full optical magnification for this condition. Figure 12 (left) shows the zoomed wrapped fringe pattern and surface image for the maximum fatigue level for a typical IIa initiation. Contour plots (right) show the maximum principal alternating (top) and mean (bottom) fatigue strains.

Figure 13 features high resolution U-field fringe patterns at minimum (left) and maximum (right) fatigue levels during initiation for a IIb loading sequence. Figure 14 is a high resolution surface image at the maximum fatigue level during initiation for a IIb loading sequence. The fatigue crack is initiating at the pinned edge of the plane intersecting the notch.

Conclusion

We have demonstrated an experimental technique for measuring local strain in superelastic Nitinol enabling us to quantify the effects of important factors relevant to the prediction of fatigue crack initiation periods for superelastic Nitinol components. The technique of phase shifted moiré interferometry was extended to acquire in situ fatigue data and shown to provide exceptional spatial and temporal resolution over a wide range of deformations.

We observed that the local strain fields at a notch in superelastic Nitinol are complex and evolve with applied loading. The effect of constraint establishes strong local stress gradients, leading to phase transformation and complex interactions between mixed phases of the material. Moving phase boundaries with singular stresses at the free surface of the specimen interact with the microstructure of the material in the notch root. This complicates the traditional methods for modifying the strain life equations to account for factors such as mean strain, multiaxial loading and the consequences of different loading amplitudes and histories that are inevitably experienced in vivo.

For samples fatigue tested with high amplitude pre-load cycles, higher cyclic amplitudes were required to initiate fatigue cracks, compared to samples that did not receive pre-loading. This effect was particularly noticeable for samples that were fatigue cycled immediately after the peak application of the high-amplitude cycles. Samples that received initial high-amplitude cycles but that were fully unloaded prior to high cycle fatigue had longer lives than the baseline, but there was more variation in the fatigue crack initiation periods.

These results were selected as a case study to show the extensibility of our approach to the general opportunity to generate data and improve understanding of the factors affecting the fatigue crack iniation in superelastic Nitinol. By utilizing samples produced from tubing, we have demonstrated a technique that has great utility for medical devices and their applications.

The design of a single sample geometry capable of being tested in both simple uniaxial tension and pure four point bending enabled us to explore differences between alternative loading configurations with a high degree of consistency.

We anticipate the application of our approach to both general studies and to improve end-use material characterization, numerical modeling, design optimization and validation.

References

[1] S.S. Manson and G.R. Halford. *Fatigue and Durability of Structural Materials*. ASM International, 2006.

[2] R.M. Tabanli, N.K. Simha, and B.T. Berg. Mean stress effects on fatigue of NiTi. *Mater. Sci. and Eng.*, A273–275:644–648, 1999.

[3] A.R. Pelton. Nitinol fatigue: A review of microstructures and mechanisms. *Journal of Materials Engineering and Performance*, 20(4–5):5, 2011.

[4] C. Kugler, D. Matson, and K.E. Perry. Non-zero mean fatigue test protocol for NiTi. In *SMST-2000: Proceedings of the International Conference on Shape Memory and Superelastic Technologies, eds. S.M. Russell and A.R. Pelton, (Pacific Grove, California: International Organization on SMST, 2001)*, pages 409–417, 2001.

[5] A.R. Runciman, D. Xu, A.R. Pelton, and R.O. Ritchie. An equivalent strain/coffin–manson approach to multiaxial fatigue and life prediction in superelastic nitinol medical devices. *Biomaterials*, 2011. doi: 1016/j.biomaterials.2011.03.057.

[6] X.-Y. Gong, D.J. Chwirut, M.R. Mitchell, and B.D. Choules. Fatigue to fracture: An informative, fast and reliable approach for assessing medical implant durability. *Journal of ASTM international*, 6(7):10, 2009.

[7] K.E. Perry, P.E. Labossiere, and E.S. Steffler. Thermoelastic transformation behavior of nitinol. In M.R. Mitchell and K.L. Jerina, editors, *Fatigue and Fracture of Medical Metallic Materials and Devices*, pages 24–33. American Society for Testing and Materials, Conshohocken, PA, 2007. ASTM STP 1481.

[8] K.E. Perry, P.E. Labossiere, and E. Steffler. Measurement of deformation and strain in nitinol. *Experimental Mechanics*, 43(3):373–380, 2007.

[9] K.E. Perry and P.E. Labossiere. Phase transformations in Nitinol and challenges for numerical modelling. In *Medical Device Materials II*, pages 131–134. ASM International, 2004.

[10] B.T. Neyer. A D-Optimality Based Sensitivity Test, 1994.

[11] D. Post, B. Han, and P. Ifju. *High Sensitivity Moiré*. Springer-Verlag, 1994.

[12] K.E. Perry. Delamination and damage in composite materials using phase-shifting moiré interferometry. *Optics and lasers in Engineering*, 24:467–483, 1996.

[13] V.A. Deason and M.B. Ward. A compact portable difraction moiré inerferometer. In *Laser Interferometry: Quantitative Analysis of Interferograms*, volume 1162, pages 26–35. SPIE, Bellingham, Washington, 1989.
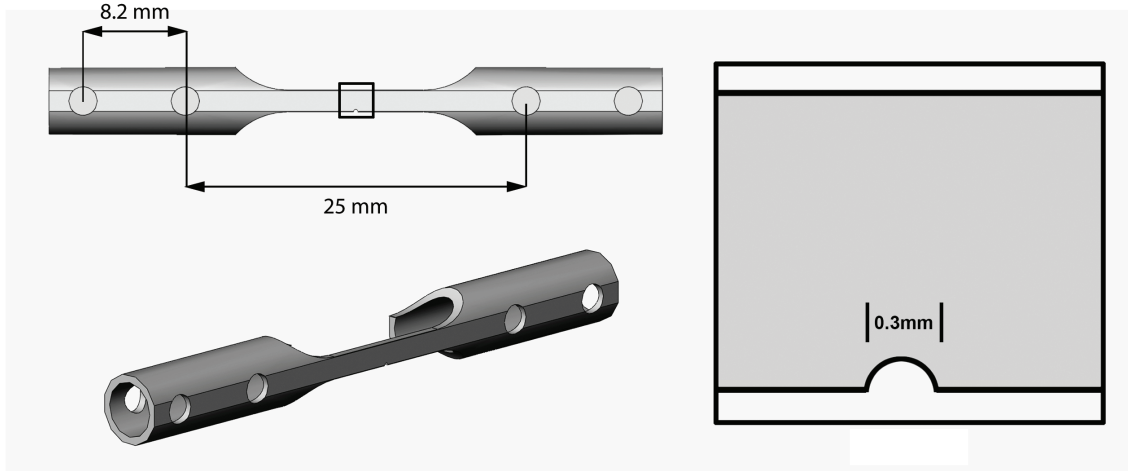
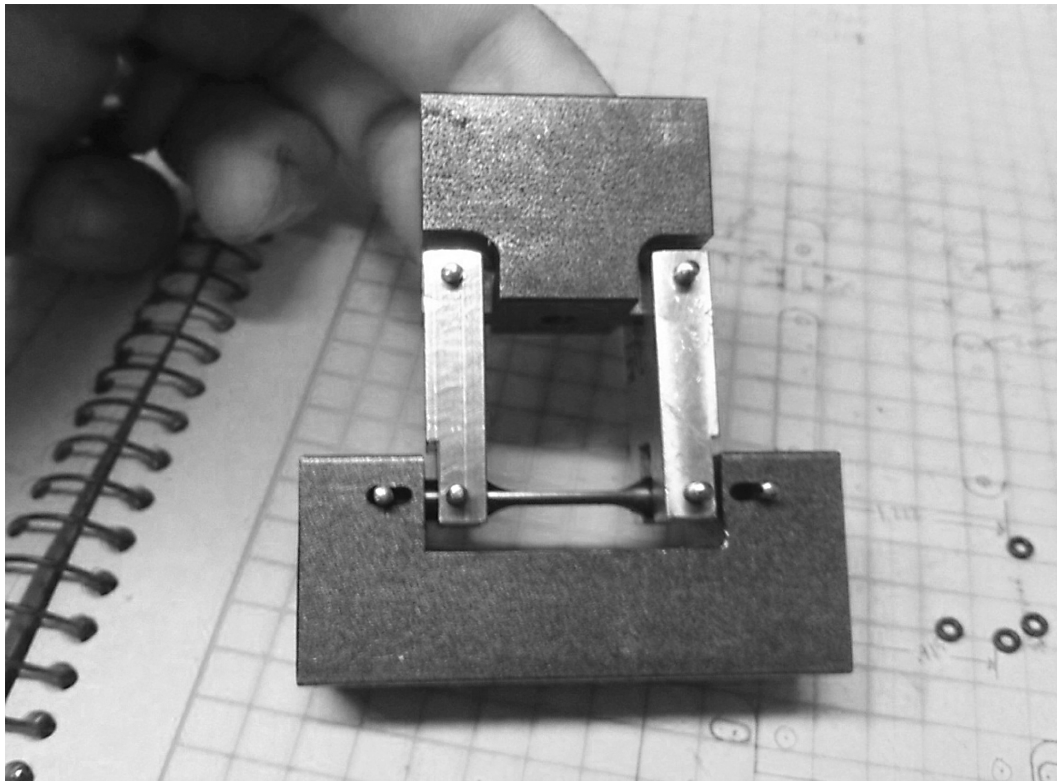Figure 1: Schematic diagram of the test sample.

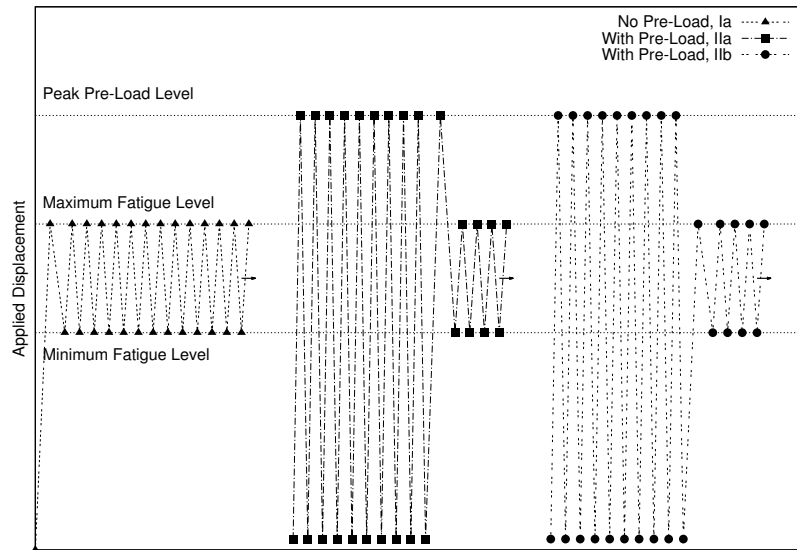Figure 2: Precision machined four point bend fatigue test fixture.

Figure 3: Schematic diagram of the three loading sequences.

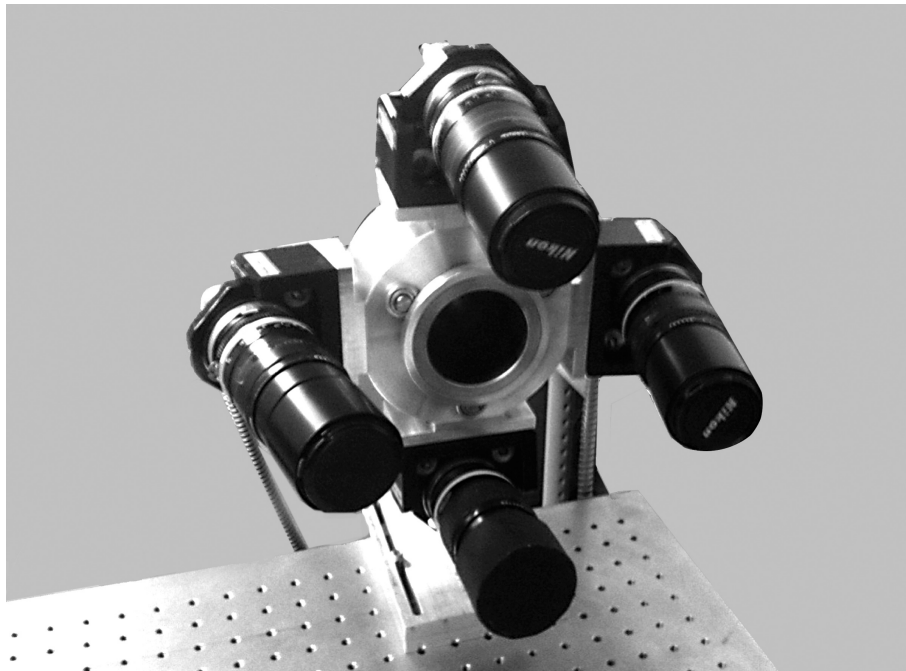Figure 4: Sample and fixture installed in the Bose 3230 dynamic test machine.

Figure 5: Four beam phase shifted moiré interferometer mounted on the optical table.
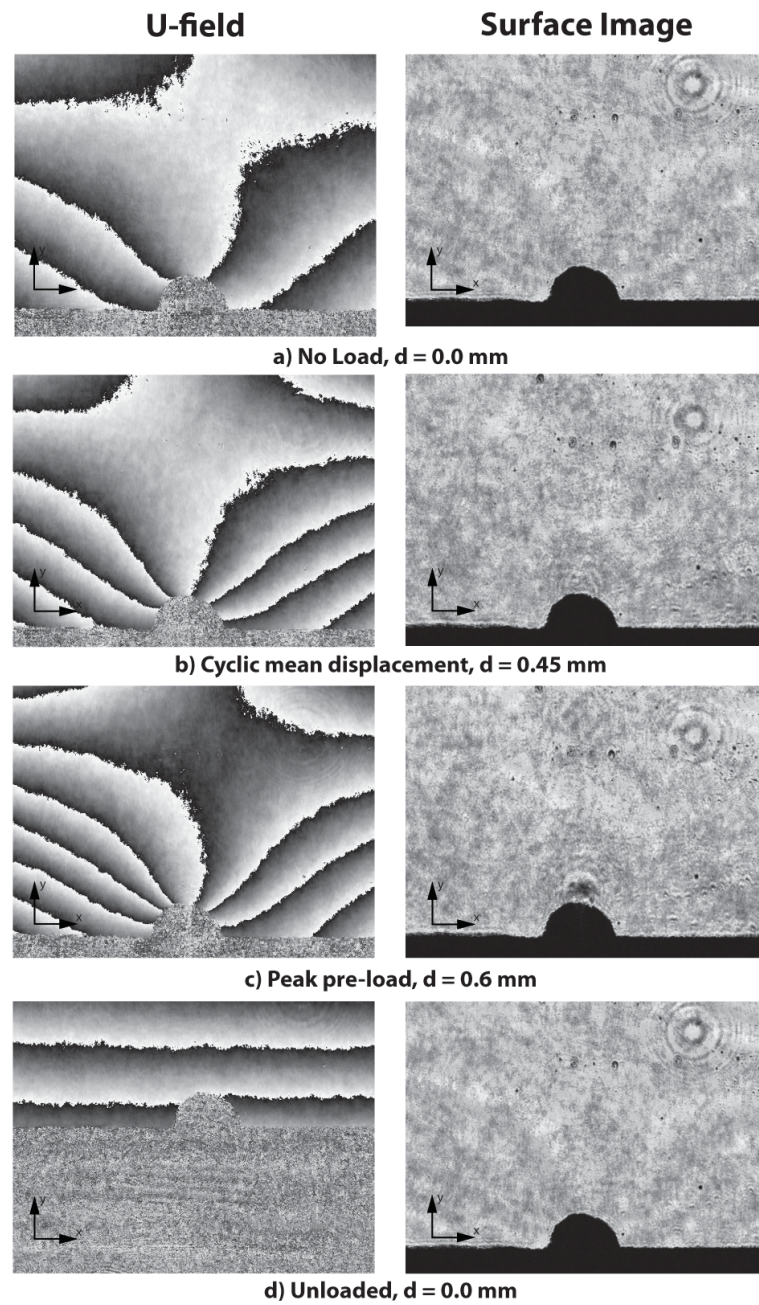
U-field   **Surface Image**

a) No Load, d = 0.0 mm

b) Cyclic mean displacement, d = 0.45 mm

c) Peak pre-load, d = 0.6 mm

d) Unloaded, d = 0.0 mm

Figure 6: Sequence of U-field fringe patterns (left) and surface images (right) for applied loading up to peak pre-load (third row) and subsequently fully unloaded (fourth row) for the first pre-load cycle.
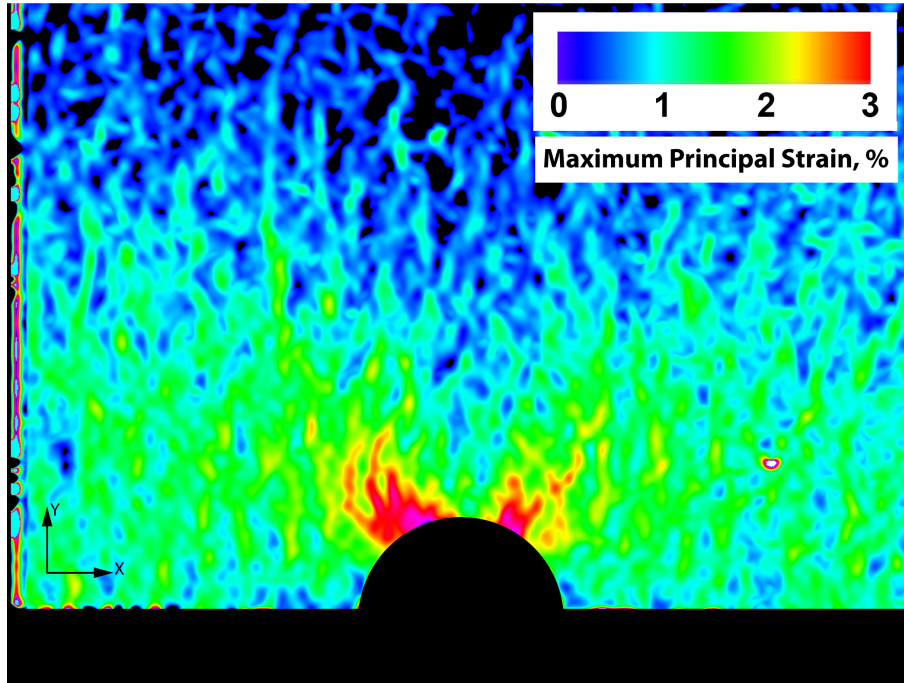
Figure 7: Contour plot of the maximum principal strain acquired at the peak pre-load level.
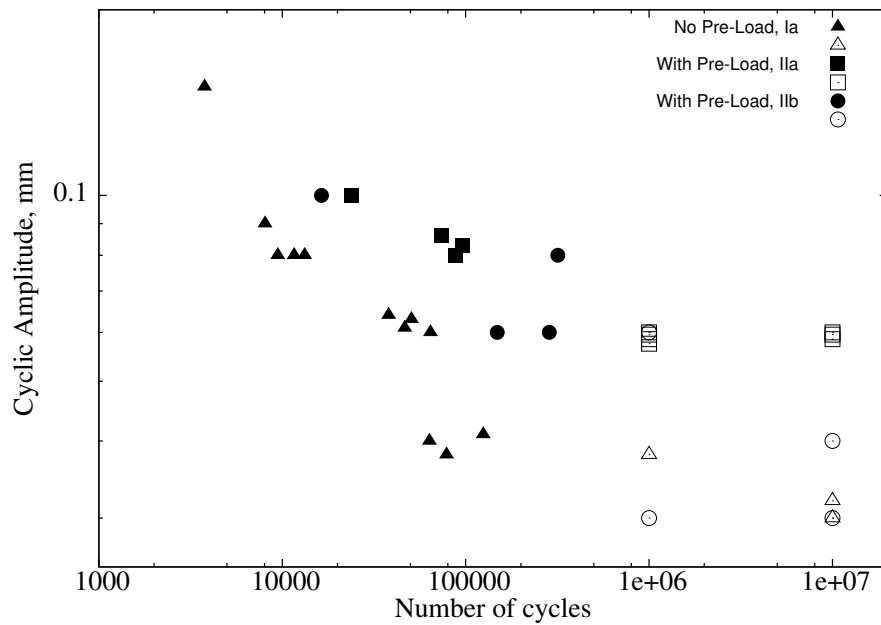
Figure 8: Cyclic amplitude/fatigue crack initiation period data for the three loading sequences. Open symbols indicate sample run out.

U-field   **Surface Image**

a) N = 62,500

b) N = 63,500

c) N = 63.500

d) N = 64,000
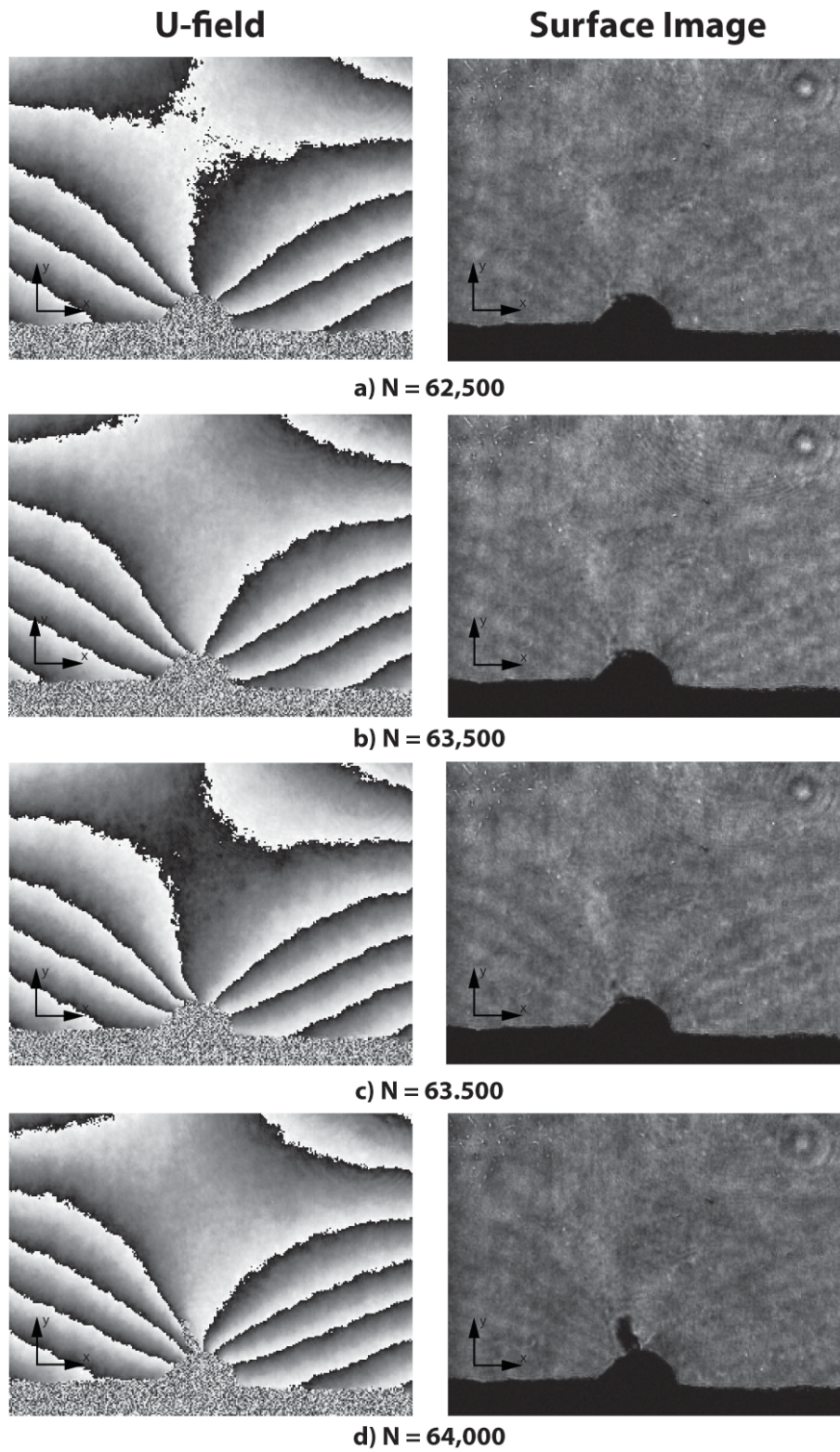
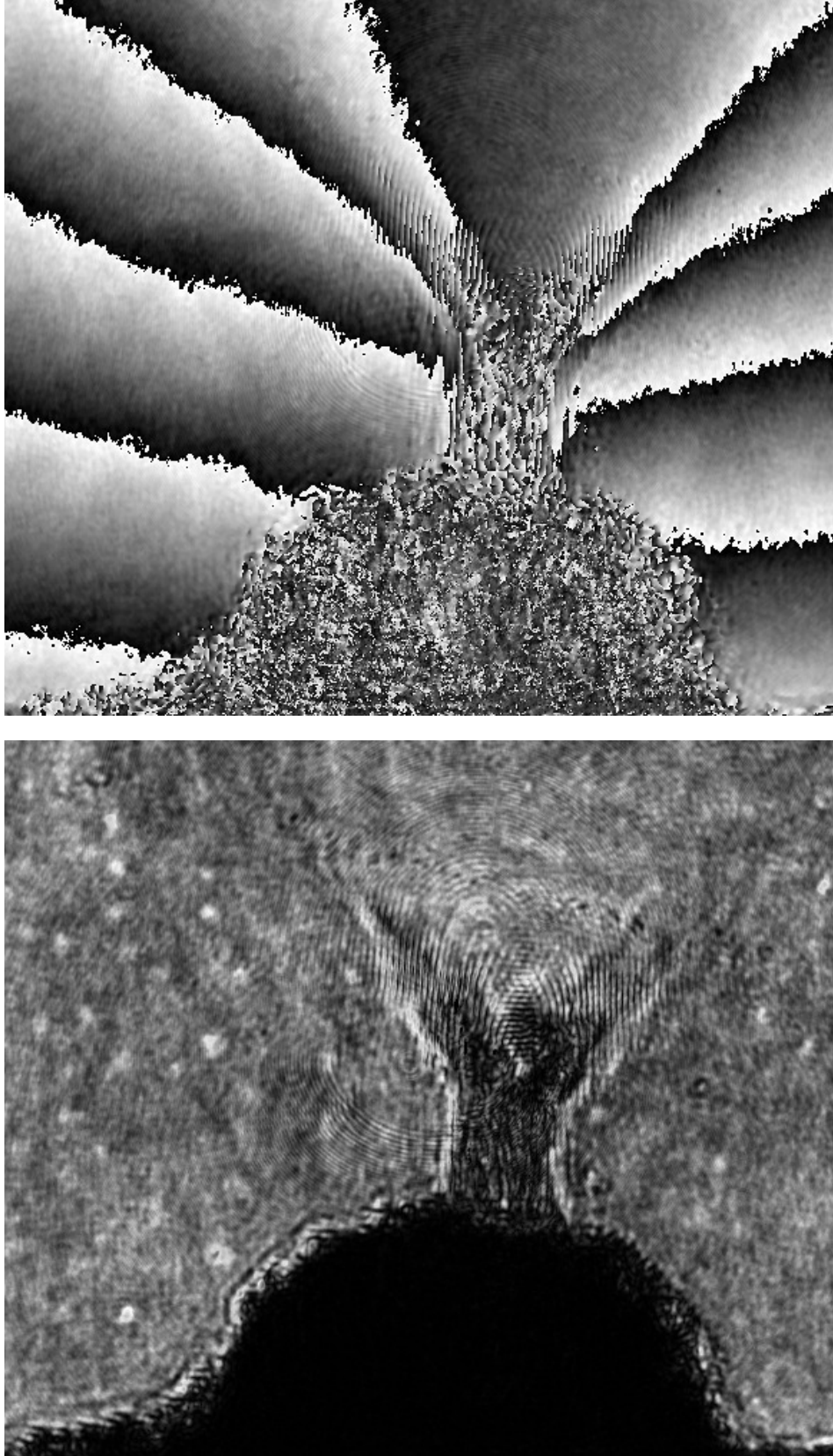Figure 9: Series of U-field fringe patterns (left) and surface images (right) acquired in situ at the maximum fatigue level during crack initiation for a Ia loading sequence.

Figure 10: High resolution U-field fringe pattern (top) and surface image (bottom) for a typical fatigue crack.
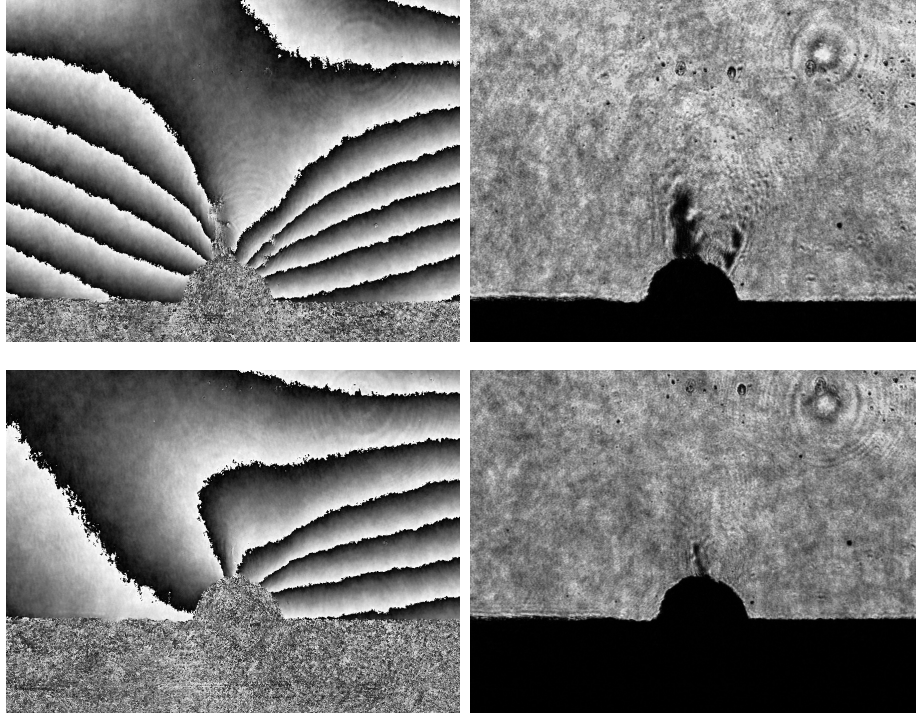
Figure 11: U-field fringe patterns and surface images at the maximum and minimum fatigue levels during initiation for a IIa loading sequence.
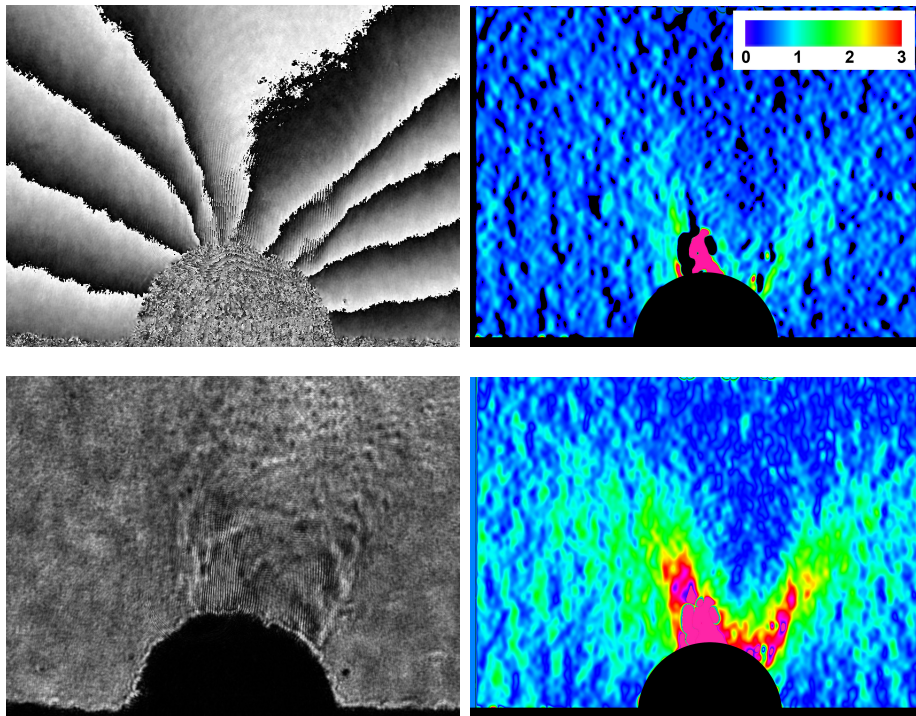

Figure 12: High resolution U-field fringe pattern and surface image at the maximum fatigue level during initiation for a IIa loading sequence. Contour plots of alternating (top) and mean strain (bottom) for this fatigue cycle are shown on the right.
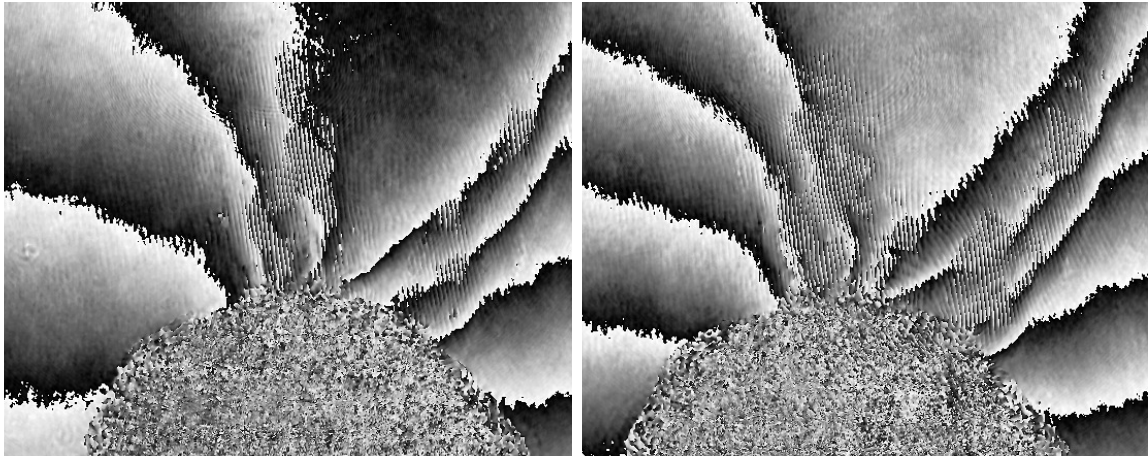
Figure 13: High resolution U-field fringe patterns at the minimum (left) and maximum (right) fatigue levels during initiation for a IIb loading sequence.
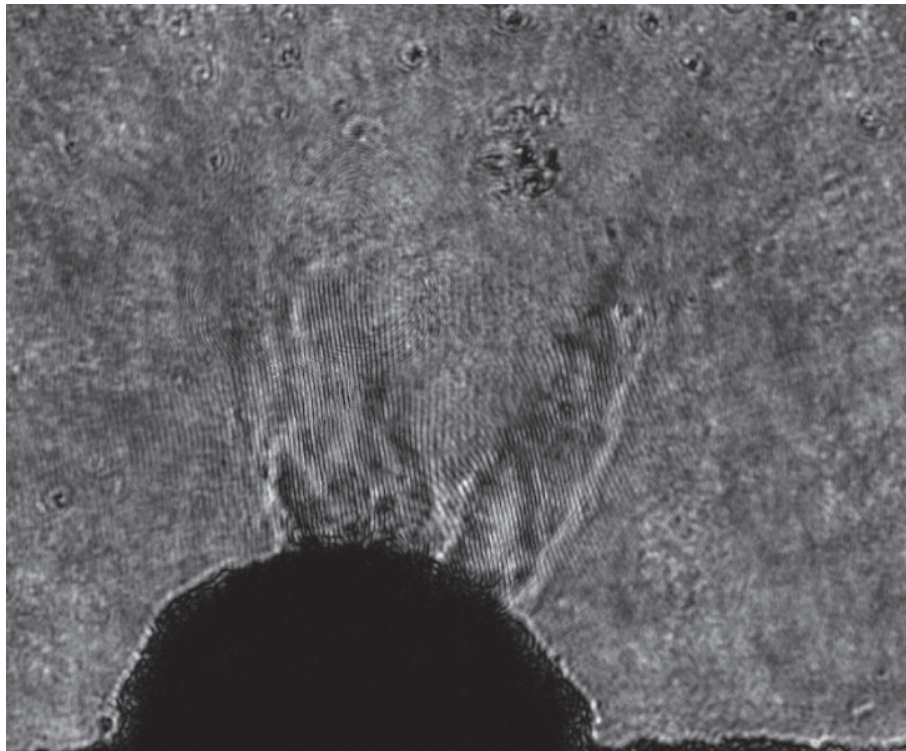

Figure 14: High resolution surface image at the maximum fatigue level during initiation for a IIb loading sequence.